



# Enhancing Cu-EDTA decomplexation in a discharge plasma system coupled with nanospace confined iron oxide: Insights into electron transfer and high-valent iron species

Yue Liu<sup>a,d</sup>, Yueyun Yang<sup>a</sup>, Anjie Li<sup>c</sup>, Jian Zhou<sup>a,d</sup>, Ying Zhang<sup>b</sup>, Tiecheng Wang<sup>a,d,\*</sup>, Hanzhong Jia<sup>a,d</sup>, Lingyan Zhu<sup>e</sup>

<sup>a</sup> College of Natural Resources and Environment, Northwest A&F University, Yangling, Shaanxi Province 712100, PR China

<sup>b</sup> College of Information Science and Technology, Nanjing Forestry University, Nanjing 210037, PR China

<sup>c</sup> College of Grassland Agriculture, Northwest A&F University, Yangling, Shaanxi 712100, PR China

<sup>d</sup> Key Laboratory of Plant Nutrition and the Agri-environment in Northwest China, Ministry of Agriculture, Yangling, Shaanxi 712100, PR China

<sup>e</sup> Ministry of Education Key Laboratory of Pollution Processes and Environmental Criteria, Tianjin Key Laboratory of Environmental Remediation and Pollution Control, College of Environmental Science and Engineering of Nankai University, Tianjin 300350, PR China

## ARTICLE INFO

### Keywords:

Nanospace confinement  
Discharge plasma  
Electron rearrangement  
Cu-EDTA  
Fe<sub>2</sub>O<sub>3</sub>

## ABSTRACT

Decomplexation of heavy metal-organic complexes dominated by reactive oxygen species (ROS) oxidation had attracted extensive attention. Nanospace confinement is a novel strategy to enhance pollutant removal due to its regulation on ROS transformation and local accelerated dynamics. Herein, nano-confined Fe<sub>2</sub>O<sub>3</sub> catalyst supported by carbon nanotubes (Fe<sub>2</sub>O<sub>3</sub>-in-CNTs) was synthesized, and it displayed obvious synergistic effects on decomplexation of Cu-EDTA complex in a non-thermal plasma (NTP) process. Cu-EDTA decomplexation efficiency reached 98.8% within 20 min in the NTP/Fe<sub>2</sub>O<sub>3</sub>-in-CNTs system, and the corresponding kinetic constant was 4.5 and 2.5 times as that in single NTP and unconfined systems, respectively. Based on experimental and theoretical results, nanospace confinement induced electron localization around Fe and C atoms and rearrangement of orbital electrons, favoring strongly oxidative Fe<sup>IV</sup> formation and catalytic decomposition of H<sub>2</sub>O<sub>2</sub> and O<sub>3</sub>. Nanospace confinement made Cu-EDTA decomplexation process transform from radical pathway to non-radical pathway. Cu-EDTA decomplexation pathways in the NTP/Fe<sub>2</sub>O<sub>3</sub>-in-CNTs were proposed.

## 1. Introduction

Heavy metals have drawn great public attention recent years because they are non-biodegradable and tend to accumulate in living organisms through food chains [1,2]. Furthermore, a large amount of organic carboxylic acid compounds coexisting in industrial effluents, such as citric acid and ethylene diamine tetraacetic acid (EDTA), are prone to chelate with the heavy metals to form stable and strongly mobile heavy metal complexes (Ni-EDTA, Cu-EDTA, and Cr-EDTA, etc.) [3,4]. Regrettably, conventional chemical precipitation processes are ineffective to remove these heavy metal complexes [5,6]. Hence, it is important to develop effective strategies to remove these complexes.

Advanced oxidation processes (AOPs) are booming developed to treat heavy metal complexes, such as Fenton [7], ozonation [8], photocatalytic oxidation [9], persulfate oxidation [10], and electrochemical

oxidation [11]. In these advanced oxidation processes, reactive oxygen species (ROS) are inclined to attack metal-organic bonds in the heavy metal complexes. Compared with these AOPs, non-thermal plasma (NTP) technology is relatively efficient and eco-friendly, and considered as a promising strategy to decompose most of stubborn organic contaminants [12,13]. Satisfactorily, various active substances are instantaneously generated without external catalysts during the NTP process, including •OH, O<sub>2</sub>•<sup>-</sup>, <sup>1</sup>O<sub>2</sub>, H<sub>2</sub>O<sub>2</sub>, O<sub>3</sub>, and high-energy electrons (e<sup>\*</sup>) [13]. A previous study also proved that the NTP system was an effective strategy to remove Cu-EDTA [14]. However, disadvantages of incomplete oxidation and low energy utilization of single NTP system limit its development and application [15,16]. In addition, long-life H<sub>2</sub>O<sub>2</sub> and O<sub>3</sub> generated in the NTP system are usually insufficiently utilized [17].

To break through those bottlenecks, various catalysts are introduced into the NTP system to enhance pollutant removal efficiency, either by

\* Corresponding author at: College of Natural Resources and Environment, Northwest A&F University, Yangling, Shaanxi Province 712100, PR China.

E-mail address: [wangtiecheng2008@126.com](mailto:wangtiecheng2008@126.com) (T. Wang).

<https://doi.org/10.1016/j.apcatb.2024.123717>

Received 12 April 2023; Received in revised form 1 December 2023; Accepted 6 January 2024

Available online 10 January 2024

0926-3373/© 2024 Elsevier B.V. All rights reserved.

integrating catalysts or by enhancing the catalytic conversion of  $\text{H}_2\text{O}_2$  and  $\text{O}_3$  to ROS [18]. Recently, iron oxides ( $\text{Fe}_2\text{O}_3$ ,  $\text{Fe}_3\text{O}_4$ , and  $\text{FeOOH}$ , etc) are promising to be used to catalyze  $\text{H}_2\text{O}_2$  by forming Fenton-like system, which are also great catalytic materials promoting the catalytic decomposition of  $\text{O}_3$  [19,20]. Nonetheless, the performance of iron oxide catalysts is easily confined by the decrease in catalytic active sites because of the loss of iron and flocculation reunion [21]. Furthermore, the catalytic activities significantly depend on the capacities of electron transport and mass transfer of catalysts [22]. Therefore, it is necessary to construct a more stable and efficient catalyst model to improve the performance of the NTP coupled with iron oxide catalysts.

Nanospace confinement is an emerging strategy to enhance the redox processes, which minimizes the space of ions or molecules to the catalyst surface by confining nanoparticles within nanospace, changing localized electron states, and expediting the kinetics of redox reactions [23,24]. Besides, nanospace confined environment can provide countermeasures to reduce the leaching of metal ions from catalysts and the interference of macromolecular components. Carbon nanotubes (CNTs) are commonly used as carbon-based catalytic materials, with unique hollow porous structure, abundant electrons and functional groups, providing superior nanospace confined conditions [25]. Zhu et al. reported that CNTs coupled with ferrihydrite accelerated electron transfer in processes of  $\text{Fe(II)/Fe(III)}$  cycle and  $\text{H}_2\text{O}_2$  activation reactions, enhancing bisphenol A removal [25]. Encapsulating Fe particles in CNTs promoted electron transfer between  $\text{Fe}^0$  and CNTs, which enhanced  $\bullet\text{OH}$  generation and favored phenolic compound removal [26]. Interestingly, CNTs confined  $\text{Fe}_2\text{O}_3$  ( $\text{Fe}_2\text{O}_3$ -in-CNTs) served as cathode in an electrochemical system promoted the in-situ generation and conversion of  $\text{H}_2\text{O}_2$  via two-electron oxidation and reduction reactions [27]. The nanospace confined materials also altered the conversion of radical oxidation pathway to non-radical pathway [27,28]. However, generative regulation of high-valent iron species (important non-radical pathway) and localized electron states induced by CNTs-confined conditions are currently underestimated. In addition, the underlying enhancement effects and mechanisms (especially for localized electron states) of NTP coupled with CNTs-confined catalysts for heavy metal complex decomposition are still unknown.

Herein, a catalytic system of NTP coupling with nanospace confined iron oxide ( $\text{Fe}_2\text{O}_3$ -in-CNTs) was established to explore its performance for Cu-EDTA decomplexation. First, the chemical structures, catalytic properties, and electron transfer capacity of  $\text{Fe}_2\text{O}_3$ -in-CNTs were characterized. Then, the performances of NTP/ $\text{Fe}_2\text{O}_3$ -in-CNTs for Cu-EDTA decomplexation were evaluated. Subsequently, the synergistic mechanisms of NTP/ $\text{Fe}_2\text{O}_3$ -in-CNTs, involving adsorption and replacement, ROS contributions, electron localization and rearrangement promoting ROS conversion based on DFT calculation, and Cu-EDTA decomposition processes, were systematically investigated. Finally, the stability and applicability of NTP/ $\text{Fe}_2\text{O}_3$ -in-CNTs on various pollutant removal in different water matrix were evaluated.

## 2. Experimental section

### 2.1. Chemicals

2,2,6,6-Tetramethylpiperidine (TEMP) and 5,5-dimethyl-1-pyrroline N-oxide (DMPO) were bought from Shanghai Maclin Biochemical Technology Co., LTD. Analytically pure ethylene diamine tetraacetic acid (EDTA), methyl phenyl sulfone (PMSO<sub>2</sub>), cupric sulfate ( $\text{CuSO}_4$ ), ferric nitrate nine hydrate ( $\text{Fe}(\text{NO}_3)_3 \cdot 9\text{H}_2\text{O}$ ), tertiary butanol (TBA), monochloroacetic acid (MA), furfuryl alcohol (FFA), potassium bromate ( $\text{KBrO}_3$ ), methyl orange (MO), nitrobenzene (NB), phenol, sulfadiazine (SD), ciprofloxacin (CIP), methyl phenyl sulfoxide (PMSO), and methylene blue (MB) were bought from Sinopharm Chemical Reagent Co., Ltd. China. Multiwalled carbon nanotube (CNTs, 10–20 nm diameter, 10–30  $\mu\text{m}$  length) was purchased from Nanfang Xianfeng Nanomaterial Technology Co. LTD.

### 2.2. Synthesis and characterization of nanospace confined materials

$\text{Fe}_2\text{O}_3$ -out-CNTs and  $\text{Fe}_2\text{O}_3$ -in-CNTs with different Fe loads were prepared according to previous study [27], as introduced in Text S1 in Supporting information. Different kinds of nanospace confined materials  $\text{Fe}_2\text{O}_3(\text{X})$ -in-CNTs were prepared, and X was the mass dosage of Fe ( $\text{NO}_3$ )<sub>3</sub>•9  $\text{H}_2\text{O}$ . As the control, unconfined catalysts ( $\text{Fe}_2\text{O}_3(\text{X})$ -out-CNTs) were also synthesized in the similar way.

The morphology of the raw CNTs and pre-treated CNTs was observed using a transmission electron microscope (TEM, HT7700, Hitachi). The high-angle annular dark-field scanning transmission electron microscope (HAADF-STEM, FEI-TALOS-F200X, Thermo) with a Super-X EDS was used to detect states of catalysts. Chemical structures and crystal types of catalysts were analyzed by X-ray photoelectron spectroscopy (XPS, Thermo Fisher) and X-ray diffraction (XRD, D8 ADVANCE A25, Bruker). The Raman pattern was performed by a Fischer DXR (Thermo, United states). The specific surface area of catalysts was obtained using a full automatic specific surface and porosity analyzer (BET, Micromeritics ASAP2460). The Fe K-edge was analyzed by X-ray absorption spectroscopy (XAS) at the Shanghai Synchrotron Radiation Facility (SSRF, Shanghai). Extended X-ray absorption fine structure (EXAFS) spectra, K-edge X-ray absorption near edge structure (XANES) of Fe, and the wavelet transform were further analyzed by Athena and Artemis software. Electrochemical workstation (CHI 660E, Chenhua, Shanghai) was used for electrochemical measurement, including electrochemical impedance spectroscopy (EIS), Tafel curves, linear sweep voltammetry (LSV), and cyclic voltammetry (CV) [28]. The detailed procedures were introduced in Text S2.

### 2.3. Experimental setup for pollutant removal

Cu-EDTA removal experiments were carried out in a NTP system, and the prepared catalysts of  $\text{Fe}_2\text{O}_3$ -in/out-CNTs were added to form heterogeneous reaction system. The detailed information on the experimental system is shown in Fig. S1 and Text S3. In a batch experiment, 200 mL Cu-EDTA solution with initial concentration of 0.05 mmol  $\text{L}^{-1}$  was treated, which was prepared by mixing  $\text{CuSO}_4$  and EDTA solutions with equal molar concentration. The catalyst dosage was 100 mg  $\text{L}^{-1}$  unless otherwise stated.

Other pollutants, including Fe-EDTA, SD, CIP, NB, phenol, MO, and MB, were also selected as model pollutants with individual concentration of 0.05 mmol  $\text{L}^{-1}$  to evaluate the performances of this system. As comparisons, several homogeneous (NTP/ $\text{Fe}^{2+}$  and NTP/ $\text{Fe}^{3+}$ ) and heterogeneous (NTP/CNTs and NTP/ $\text{Fe}_2\text{O}_3$ ) systems were also established. In these systems, the dosages of  $\text{Fe}^{2+}$ ,  $\text{Fe}^{3+}$ , and  $\text{Fe}_2\text{O}_3$  were consistent with the contents of Fe in  $\text{Fe}_2\text{O}_3$ -in-CNTs.

### 2.4. Other analyses

Cu-EDTA concentration was monitored using high performance liquid chromatography (HPLC) [14]. The catalytic performances on Cu-EDTA elimination were evaluated by decomplexation efficiency, the first-order kinetics, turnover frequency (TOF), turnover number (TON), and active sites, as described in Text S4 [28]. TBA, FFA, and  $\text{KBrO}_3$  were chosen as quenchers of  $\bullet\text{OH}$ ,  $^1\text{O}_2$ , and  $\text{e}^*$  to identify their contributions, respectively [14,29]. The concentrations of  $\text{H}_2\text{O}_2$  and  $\text{O}_3$  were detected by potassium oxalate-spectrophotometric method and disulphonate spectrophotometry, respectively [13,30]. Electron paramagnetic resonance (EPR) was used to detect ROS, where TEMP and DMPO were chosen as probe reagents. The generation and role of  $\text{Fe}^{\text{IV}}=\text{O}$  were semi-quantitatively analyzed by monitoring the generation of methyl phenyl sulfone (PMSO<sub>2</sub>), as described in Text S5 [31]. The steady-state concentrations of active species ( $\bullet\text{OH}$ ,  $^1\text{O}_2$ , and  $\text{Fe}^{\text{IV}}=\text{O}$ ) and their contributions were calculated by chemical probe methods, as described in Text S6. Gas chromatography-mass spectrometer (GC-MS, 7890B-5977B, Agilent) was used to identify Cu-EDTA decomposition

products [5]. In addition, Fe-EDTA, SD, CIP, NB, phenol, MO, and MB were detected as shown in Table S1. All quantitative analyses were based on the average of three tests.

### 2.5. Theoretical calculation

The density functional theory (DFT) calculation was conducted to evaluate the nanospace confinement effects. The K-points were set as  $1 \times 1 \times 1$  for bulk  $\text{Fe}_2\text{O}_3$ , with cutoff energy of 400 eV. In addition, the self-consistent field energy convergency value was set at  $1 \times 10^{-4}$  eV, and the force convergency value for atoms was 0.05 eV/Å.

## 3. Results and discussion

### 3.1. Characterization of nanospace confined catalysts

Fig. S2 shows the morphology of raw CNTs and prepared CNTs. The prepared CNTs were open-ended, while the raw CNTs were closed-ended. Fig. 1a displays the morphology of the  $\text{Fe}_2\text{O}_3(100)$ -in-CNTs, and the (110) crystalline lattice of  $\text{Fe}_2\text{O}_3$  nanoparticles was observed in HRTEM (inset in Fig. 1a). The representative HAADF-STEM images with EDX elemental mapping of C, O, and Fe explicitly showed that  $\text{Fe}_2\text{O}_3$  nanoparticles were randomly distributed in CNT channels (Fig. 1b-f). Meanwhile,  $\text{Fe}_2\text{O}_3$  nanoparticles on the outer sidewall of CNTs in the  $\text{Fe}_2\text{O}_3(100)$ -out-CNTs were clearly observed (Fig. S3). The diffraction peaks of the (110), (114), and (214) lattice planes of  $\text{Fe}_2\text{O}_3$

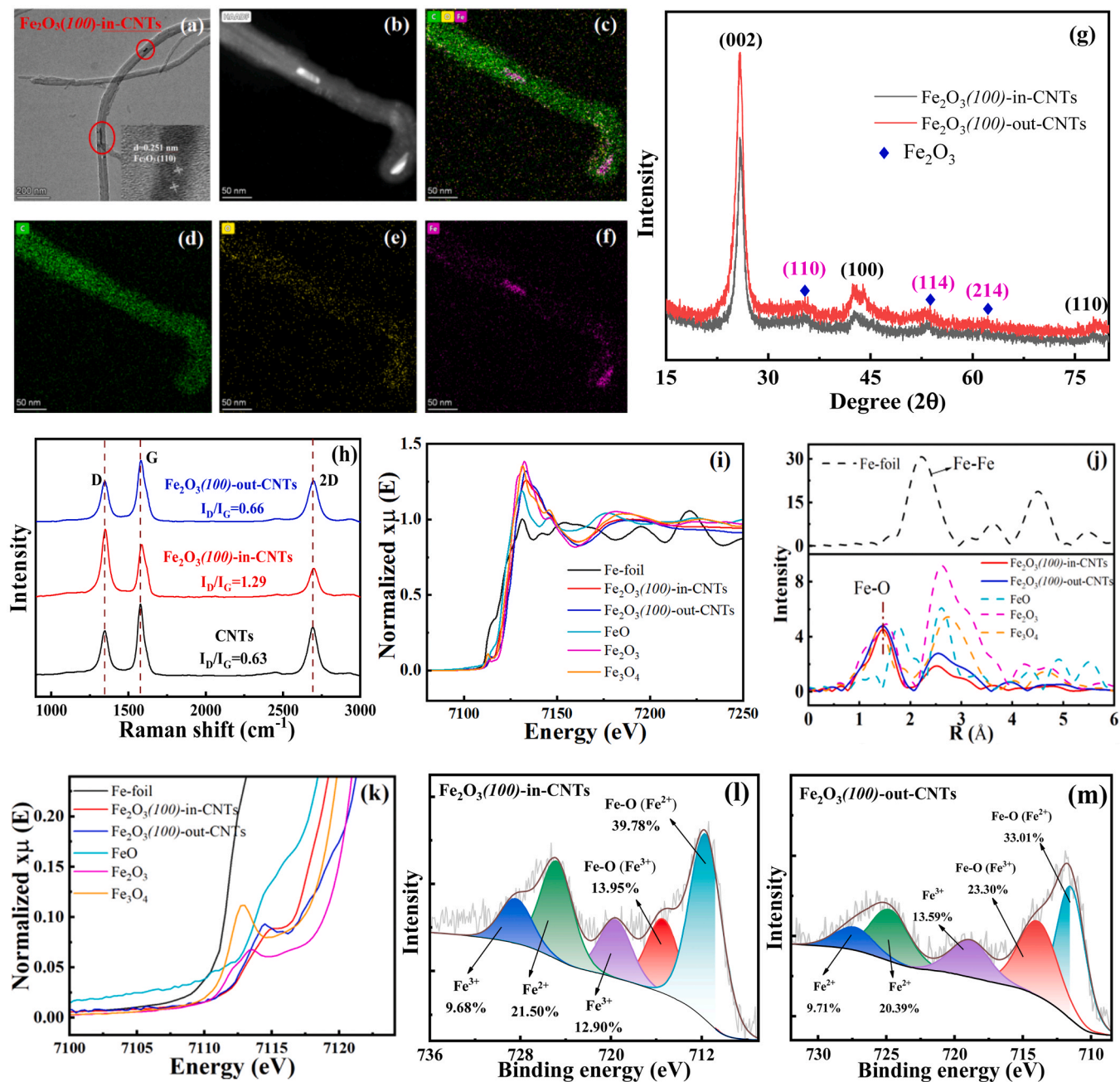
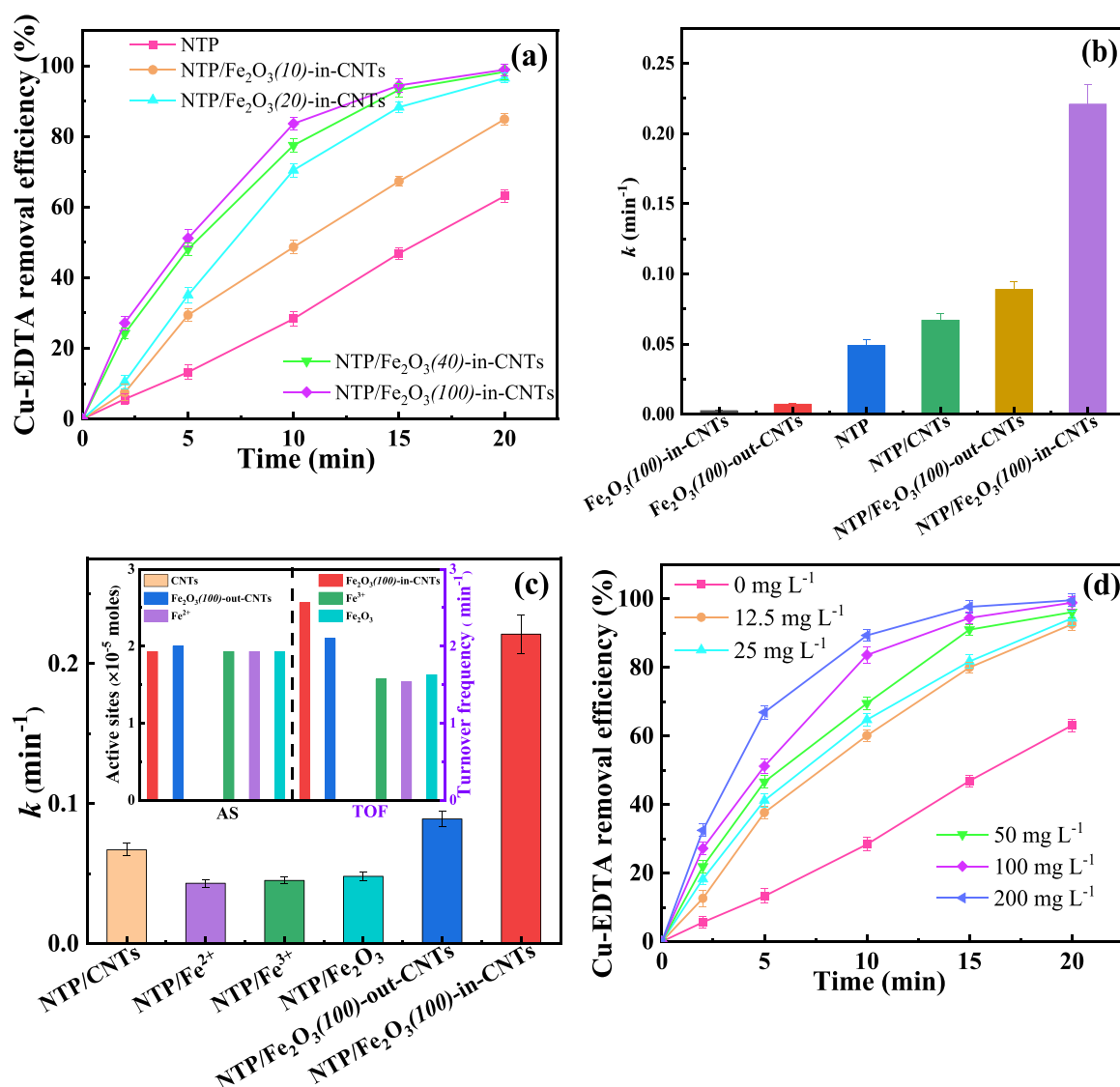


Fig. 1. HRTEM of  $\text{Fe}_2\text{O}_3(100)$ -in-CNTs (a); HAADF-STEM of  $\text{Fe}_2\text{O}_3(100)$ -in-CNTs (b); EDX mappings of  $\text{Fe}_2\text{O}_3(100)$ -in-CNTs (c-f); XRD spectra (g); Raman spectra (h); XANES spectra of Fe (i); k-edge phase-corrected Fourier transforms spectra of Fe (j); k-edge XANES spectra of Fe (k); Fe 2p XPS of  $\text{Fe}_2\text{O}_3(100)$ -in-CNTs (l) and  $\text{Fe}_2\text{O}_3(100)$ -out-CNTs (m).

(PDF#33–0664) exhibited in the  $\text{Fe}_2\text{O}_3(100)$ -in-CNTs and  $\text{Fe}_2\text{O}_3(100)$ -out-CNTs, as shown in XRD patterns (Fig. 1g). Interestingly, the diffraction peaks of the (110), (100), and (002) lattice planes of CNTs decreased with the increase of Fe content in  $\text{Fe}_2\text{O}_3$ -in-CNTs (Fig. S4a), suggesting the destruction of graphite structure. The larger value of  $I_D/I_G$  in Raman spectra of the  $\text{Fe}_2\text{O}_3(100)$ -in-CNTs (Fig. 1h and Fig. S4b) further demonstrated the disordered graphite structure and more defects, as compared with the  $\text{Fe}_2\text{O}_3(100)$ -out-CNTs [32]. Besides, there was a slight blue-shift of the D and G peaks of the  $\text{Fe}_2\text{O}_3(100)$ -in-CNTs, which was probably related to the reduction of ordered graphite structure and decreased covalent  $\pi$  electron delocalization [33]. In addition, the  $\text{Fe}_2\text{O}_3(100)$ -in-CNTs had a larger specific surface area than the  $\text{Fe}_2\text{O}_3(100)$ -out-CNTs (Table S2).

In Fig. 1i, the absorption thresholds of EXAFS spectra of catalysts were close to  $\text{Fe}_2\text{O}_3$ , demonstrating that  $\text{Fe}_2\text{O}_3$  was the main species in the unconfined and confined materials. These could also be confirmed by the occurrence of the main peak around 1.47 Å in the K-edge phase-corrected Fourier transforms EXAFS, which was associated with Fe-O bonds (Fig. 1j). Moreover, the absorption edge in XANES spectra

illustrated that the chemical states of Fe were between  $\text{Fe}^{2+}$  and  $\text{Fe}^{3+}$  (Fig. 1k). Fig. 1l and m depict the XPS spectra of Fe 2p of the  $\text{Fe}_2\text{O}_3(100)$ -in-CNTs and  $\text{Fe}_2\text{O}_3(100)$ -out-CNTs, respectively. The peaks with the binding energy around 711.68 eV, 715.48 eV, 724.78 eV, and 728.28 eV were associated with Fe-O ( $\text{Fe}^{2+}$ ), Fe-O ( $\text{Fe}^{3+}$ ),  $\text{Fe}^{2+}$ , and  $\text{Fe}^{3+}$ , respectively [25,34].  $\text{Fe}^{2+}$  occupied a higher proportion in both  $\text{Fe}_2\text{O}_3(100)$ -in-CNTs and  $\text{Fe}_2\text{O}_3(100)$ -out-CNTs, especially in the  $\text{Fe}_2\text{O}_3(100)$ -in-CNTs, which was conducive to catalysis [25,34]. Compared with the C 1s in the  $\text{Fe}_2\text{O}_3(100)$ -out-CNTs, the  $\text{sp}^2$  C-C proportion decreased and  $\pi$ - $\pi^*$  transition proportion increased in the  $\text{Fe}_2\text{O}_3(100)$ -in-CNTs (Fig. S5a and Fig. S5c), indicating that the  $\text{Fe}_2\text{O}_3(100)$ -in-CNTs probably had a better catalytic performance [27, 35]. In addition, more -COOH groups were modified in the  $\text{Fe}_2\text{O}_3(100)$ -in-CNTs compared with the  $\text{Fe}_2\text{O}_3(100)$ -out-CNTs, and thus more active sites would be provided (Fig. S5b and Fig. S5d). Overall, the nanospace confined  $\text{Fe}_2\text{O}_3(100)$ -in-CNTs were successfully synthesized and probably had greater catalytic performances.



**Fig. 2.** Effect of Fe dosage in  $\text{Fe}_2\text{O}_3$ -in-CNTs on Cu-EDTA removal (a) (Catalyst dosage = 0.1 g L<sup>-1</sup>,  $[\text{Cu-EDTA}]_0 = 0.05$  mmol L<sup>-1</sup>, Voltage = 12 kV); Cu-EDTA removal kinetics (b) (Catalyst dosage = 0.1 g L<sup>-1</sup>,  $[\text{Cu-EDTA}]_0 = 0.05$  mmol L<sup>-1</sup>, Voltage = 12 kV); comparison of the first order kinetic constants of homogeneous and heterogeneous systems, active sites (AS), and turnover frequency (TOF) (c) (Catalyst dosage = 0.1 g L<sup>-1</sup>,  $[\text{Cu-EDTA}]_0 = 0.05$  mmol L<sup>-1</sup>, Voltage = 12 kV,  $[\text{Fe}^{2+}]_0 = [\text{Fe}^{3+}]_0 = 1.08$  mg L<sup>-1</sup>,  $\text{Fe}_2\text{O}_3$  dosage = 0.5 mg L<sup>-1</sup>); effect of  $\text{Fe}_2\text{O}_3(100)$ -in-CNTs dosage on Cu-EDTA removal (d) (Voltage = 12 kV,  $[\text{Cu-EDTA}]_0 = 0.05$  mmol L<sup>-1</sup>).



### 3.2. Catalytic performance of the nanospace confined catalysts

Fig. 2a depicts the effect of Fe dosage in  $\text{Fe}_2\text{O}_3(\text{X})$ -in-CNTs on Cu-EDTA elimination. The presence of  $\text{Fe}_2\text{O}_3(\text{X})$ -in-CNTs promoted Cu-EDTA elimination, and it was enhanced with Fe dosage. In the single NTP system, Cu-EDTA removal efficiency only reached 63.1% after 20 min; it increased to 84.8% and 98.8% after adding  $\text{Fe}_2\text{O}_3(10)$ -in-CNTs and  $\text{Fe}_2\text{O}_3(100)$ -in-CNTs, respectively. These could be attributed to the higher total Fe content (Fig. S6). Fig. 2b compares the removal performances of Cu-EDTA in the  $\text{Fe}_2\text{O}_3(100)$ -in-CNTs and  $\text{Fe}_2\text{O}_3(100)$ -out-CNTs catalytic systems. The adsorption capacity of  $\text{Fe}_2\text{O}_3(100)$ -in-CNTs and  $\text{Fe}_2\text{O}_3(100)$ -out-CNTs on Cu-EDTA could be neglected because of their quite low reaction rate constants ( $0.0025$  and  $0.071 \text{ min}^{-1}$ ). Interestingly, the reaction rate constant in the  $\text{Fe}_2\text{O}_3(100)$ -in-CNTs system was 2.48 times as in the  $\text{Fe}_2\text{O}_3(100)$ -out-CNTs system. In addition, low first-order kinetic constants were observed in the conventional homogeneous (NTP/ $\text{Fe}^{2+}$  and NTP/ $\text{Fe}^{3+}$ ) and heterogeneous (NTP/CNTs and NTP/ $\text{Fe}_2\text{O}_3$ ) systems. The reaction rate constant in the NTP/ $\text{Fe}_2\text{O}_3(100)$ -in-CNTs system was approximately 5.1 folds, 4.9 folds, and 4.6 folds higher than that in the NTP/ $\text{Fe}^{2+}$ , NTP/ $\text{Fe}^{3+}$ , and NTP/ $\text{Fe}_2\text{O}_3$  systems, respectively (Fig. 2c). Moreover, turnover frequency (TOF) based on active sites was further used to investigate the catalytic performance of  $\text{Fe}_2\text{O}_3(100)$ -in-CNTs. As depicted in Fig. 2c (inset), the  $\text{Fe}_2\text{O}_3(100)$ -in-CNTs exhibited the highest TOF value ( $2.5 \text{ min}^{-1}$ ) than other catalysts, suggesting the greatest catalytic performance [36]. Li et al. synthesized a single atom iron to realize ultrafast Fenton reactions, but the TOF value was just  $1.01 \text{ min}^{-1}$  [36]. These results suggested that the nanoconfinement could effectively reduce the reaction distance and accelerated the reaction frequency, and thus significantly promoted the catalytic decomposition performance of Cu-EDTA. Fig. 2d shows the influences of  $\text{Fe}_2\text{O}_3(100)$ -in-CNTs dosage on Cu-EDTA elimination. The increase of  $\text{Fe}_2\text{O}_3(100)$ -in-CNTs dosage promoted Cu-EDTA removal, and Cu-EDTA removal efficiency reached 98.8% and 99.6% after 20 min as the  $\text{Fe}_2\text{O}_3(100)$ -in-CNTs dosage rose to 100 and  $200 \text{ mg L}^{-1}$ , respectively.

### 3.3. Synergetic mechanisms of NTP/ $\text{Fe}_2\text{O}_3(100)$ -in-CNTs

#### 3.3.1. Adsorption and replacement

Only less than 10% of Cu-EDTA was removed in the single  $\text{Fe}_2\text{O}_3(100)$ -in-CNTs adsorption system (Fig. 2b), illustrating that the adsorption effect displayed a negligible contribution to Cu-EDTA elimination. Chen et al. reported that CNTs treated by  $\text{HNO}_3$  were negatively charged, and the Fe doping also performed similar electronegativity [32]. “Cu-EDTA<sup>2-</sup>” was the dominant species at pH 4.0–10.0 (Fig. S7). Therefore, due to the electrostatic repulsion,  $\text{Fe}_2\text{O}_3(100)$ -in-CNTs had a poor adsorption capacity for Cu-EDTA.  $\text{Fe(III)}$  could replace Cu in the Cu-EDTA species due to the stronger chelating capacity of  $\text{Fe(III)}$ -EDTA [6]. However, the replacement of Fe was also inappreciable (less than 5%, Fig. S8a) because of the low Fe leaching from  $\text{Fe}_2\text{O}_3(100)$ -in-CNTs during the treatment process (below  $40 \text{ } \mu\text{g L}^{-1}$  within 20 min), as shown in Fig. S8b. The UV-vis spectra further provided evidence for the negligible replacement effect (Fig. S8c). Thus, the adsorption and replacement effects derived from  $\text{Fe}_2\text{O}_3(100)$ -in-CNTs contributed little to Cu-EDTA removal.

#### 3.3.2. Contributions of ROS

NTP can induce a variety of ROS generation, favoring elimination of pollutants [14].  $\text{O}_3$  and  $\text{H}_2\text{O}_2$  are typical long-lived ROS in the NTP process, which can react with pollutants directly or be converted to other reactive radicals [15,37]. The concentration of  $\text{H}_2\text{O}_2$  was  $0.1 \text{ } \mu\text{g L}^{-1}$  in the NTP system after 2 min of treatment (Fig. S9a), and it increased to 0.30 and  $0.35 \text{ } \mu\text{g L}^{-1}$  in the NTP/ $\text{Fe}_2\text{O}_3(100)$ -in-CNTs and NTP/ $\text{Fe}_2\text{O}_3(100)$ -out-CNTs systems without Cu-EDTA, respectively. Previous studies suggested that the surface functional groups of carbonaceous catalysts could react with  $\text{O}_3$  to form  $\text{H}_2\text{O}_2$ , and  $\text{O}_2$  could further

yield  $\text{H}_2\text{O}_2$  at the surface of carbonaceous catalysts via two-electron reduction process [38,39]. The microelectrolysis effect induced by Fe species and carbonaceous catalysts further accelerated the formation of  $\text{H}_2\text{O}_2$  [40]. In the presence of Cu-EDTA,  $\text{H}_2\text{O}_2$  concentration significantly decreased in both the NTP/ $\text{Fe}_2\text{O}_3(100)$ -in-CNTs and NTP/ $\text{Fe}_2\text{O}_3(100)$ -out-CNTs systems, demonstrating the obvious contributions of  $\text{H}_2\text{O}_2$ . As shown in Fig. S9b, the  $\text{O}_{3(\text{aq})}$  was  $3.1 \text{ mg L}^{-1}$  in the NTP system without Cu-EDTA, while it was  $2.5 \text{ mg L}^{-1}$  in the NTP/ $\text{Fe}_2\text{O}_3(100)$ -in-CNTs system. These results demonstrated the occurrence of catalytic  $\text{O}_3$  decomposition in the presence of catalyst. Moreover, there was an obvious decrease in the  $\text{O}_{3(\text{aq})}$  concentration in the NTP/ $\text{Fe}_2\text{O}_3(100)$ -in-CNTs system containing Cu-EDTA, thus  $\text{O}_{3(\text{aq})}$  played vital roles in Cu-EDTA removal. Similar phenomena were also observed in the NTP/ $\text{Fe}_2\text{O}_3(100)$ -out-CNTs system.

Quenching experiments using TBA and FFA as quenchers were further performed to disclose ROS contribution. The dosage of these quenchers was all  $100 \text{ mmol L}^{-1}$ , which was much higher than Cu-EDTA concentration. As shown in Fig. 3a, with the addition of TBA and FFA, the reaction rate constant for Cu-EDTA removal in the NTP/ $\text{Fe}_2\text{O}_3(100)$ -in-CNTs system decreased by 78.7% and 82.8%, respectively, and thus  $\bullet\text{OH}$  and  $^1\text{O}_2$  displayed significant roles in Cu-EDTA decomposition, especially for  $^1\text{O}_2$ . As a control, the addition of TBA and FFA to the NTP/ $\text{Fe}_2\text{O}_3(100)$ -out-CNTs system also led to 36.2% and 17.2% decreases in the reaction rate constants (Fig. 3b). The stronger inhibition effects in the NTP/ $\text{Fe}_2\text{O}_3(100)$ -in-CNTs system indicated that more aggressive ROS reactions occurred in the nanospace confined catalysts, compared with unconfined materials. Fig. 3c depicts EPR spectra of TEMP- $^1\text{O}_2$  and DMPO- $\bullet\text{OH}$  in different systems, and great enhancement of TEMP- $^1\text{O}_2$  signals was observed in the NTP/ $\text{Fe}_2\text{O}_3(100)$ -in-CNTs system, reflecting more  $^1\text{O}_2$  formation in a nanospace confinement environment [28]. Inversely, higher signal intensity of DMPO- $\bullet\text{OH}$  was observed in the NTP/ $\text{Fe}_2\text{O}_3(100)$ -out-CNTs system, demonstrating important role of  $\bullet\text{OH}$  in an unconfined space [27,28].

High-valent iron ( $\text{Fe}^{\text{IV}}=\text{O}$ ), another active species with a strong oxidation potential ( $E_0(\text{Fe}^{\text{IV}}/\text{Fe}^{\text{III}}) = 1.8 \text{ eV}$ ) and selectivity, is usually formed in the Fe-based oxidation processes [41,42]. The  $\text{Fe}^{\text{IV}}=\text{O}$  can selectively transform PMSO to  $\text{PMSO}_2$ , hence PMSO is commonly selected to confirm its formation [31]. As shown in Fig. 3d, after 20 min reaction, 1.4 and  $1.0 \text{ } \mu\text{mol L}^{-1}$  of  $\text{PMSO}_2$  were generated in the NTP/ $\text{Fe}_2\text{O}_3(100)$ -in-CNTs and NTP/ $\text{Fe}_2\text{O}_3(100)$ -out-CNTs systems, respectively. Furthermore, Cu-EDTA removal kinetics were also monitored with PMSO addition in the nanospace confined and unconfined systems. As shown in Fig. 3a-b, obvious decline in the reaction rate constant was observed in the NTP/ $\text{Fe}_2\text{O}_3(100)$ -in-CNTs system after adding PMSO, while negligible change occurred in the NTP/ $\text{Fe}_2\text{O}_3(100)$ -out-CNTs system. Thus, more  $\text{Fe}^{\text{IV}}=\text{O}$  species was produced in the NTP/ $\text{Fe}_2\text{O}_3(100)$ -in-CNTs system and contributed to Cu-EDTA removal. Generally, the  $\text{Fe}^{\text{IV}}=\text{O}$  species mainly destroyed pollutants through electrophilic attack or electron transfer [42]; meanwhile, the capacity of electron transfer would be enhanced, resulting in more multiple active species formation (such as  $\bullet\text{OH}$  and  $^1\text{O}_2$ ) [42]. Thus, better Cu-EDTA decomposition efficiency was observed in the NTP/ $\text{Fe}_2\text{O}_3(100)$ -in-CNTs system.

The steady-state concentrations of active species were further calculated. As depicted in Fig. 3e and Table S3, fast removal kinetics of FFA was realized in the NTP/ $\text{Fe}_2\text{O}_3(100)$ -in-CNTs system with a high  $k_{\text{app,FFA}}$  of  $1.11 \text{ min}^{-1}$ , but it was  $0.11 \text{ min}^{-1}$  and  $0.023 \text{ min}^{-1}$  for  $k_{\text{app,NB}}$  and  $k_{\text{app,PMSO}}$ , respectively. Correspondingly, the steady-state concentrations of  $\bullet\text{OH}$ ,  $^1\text{O}_2$ , and  $\text{Fe}^{\text{IV}}=\text{O}$  species were  $6.2 \times 10^{-13}$ ,  $1.5 \times 10^{-10}$ , and  $3.2 \times 10^{-9} \text{ mol L}^{-1}$  in the NTP/ $\text{Fe}_2\text{O}_3(100)$ -in-CNTs system, respectively, which were higher than those in the NTP/ $\text{Fe}_2\text{O}_3(100)$ -out-CNTs system (Fig. S10). In addition, obvious decreases in Cu-EDTA removal efficiency were observed in the NTP/ $\text{Fe}_2\text{O}_3(100)$ -in-CNTs system when chemical probes of  $\bullet\text{OH}$  and  $^1\text{O}_2$  were added, as well as the first-order rate constants (Fig. S11a and Table S4). Fig. 3f depicts the contributions (f) of these active species. 34.5%, 36.2%, and 29.3% of

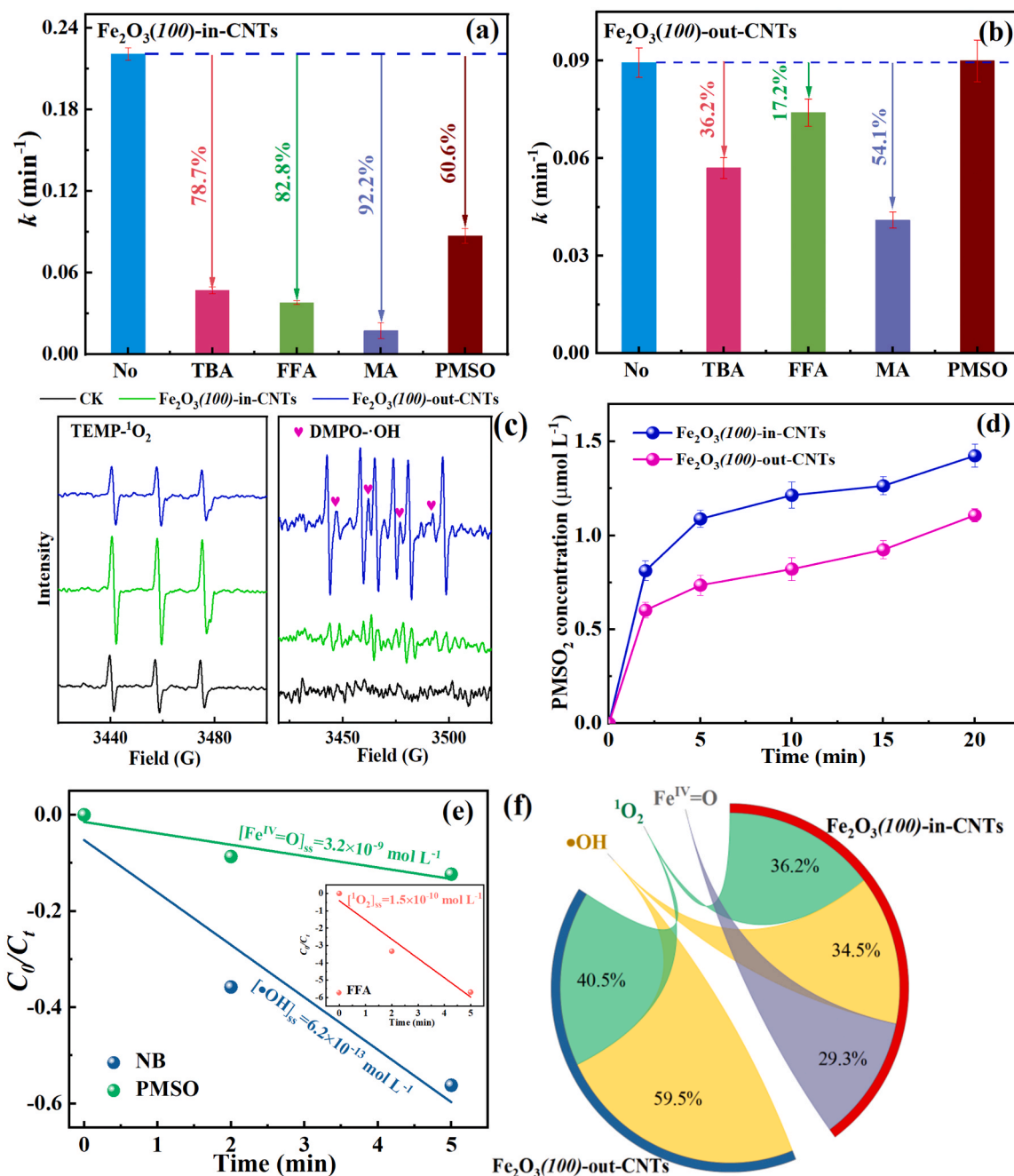


**Fig. 3.** First order kinetic constants of Cu-EDTA elimination with different scavengers in NTP/Fe<sub>2</sub>O<sub>3</sub>(100)-in-CNTs system (a) and NTP/Fe<sub>2</sub>O<sub>3</sub>(100)-out-CNTs system (b) ([PMSO]<sub>0</sub> = 0.05 mmol L<sup>-1</sup>, [TBA]<sub>0</sub> = [FFA]<sub>0</sub> = [MA]<sub>0</sub> = 100 mmol L<sup>-1</sup>); EPR spectra of TEMP-<sup>1</sup>O<sub>2</sub> and DMPO-•OH (c) ([TEMP] = [DMPO] = 10 mmol L<sup>-1</sup>); changes in PMSO<sub>2</sub> concentration in different systems (d); steady-state concentration of ROS in NTP/Fe<sub>2</sub>O<sub>3</sub>(100)-in-CNTs system (e) ([PMSO]<sub>0</sub> = 0.05 mmol L<sup>-1</sup>, [NB]<sub>0</sub> = [FFA]<sub>0</sub> = 0.01 mmol L<sup>-1</sup>); contributions of ROS (f).

contributions were attributed to •OH, <sup>1</sup>O<sub>2</sub>, and Fe<sup>IV</sup>=O species for Cu-EDTA removal in the NTP/Fe<sub>2</sub>O<sub>3</sub>(100)-in-CNTs system, respectively. However, •OH dominated Cu-EDTA removal in the NTP/Fe<sub>2</sub>O<sub>3</sub>(100)-out-CNTs system, with much higher contribution of 59.5% (Fig. 3f). Previous study also reported that non-radical pathway dominated pollutant degradation processes in the nanospace confined system, while radical pathway dominated in the unconfined system [27].

### 3.3.3. Electron transfer

CNTs can accelerate the electron transfer at the reaction interface in the heterogeneous system, promoting pollutant removal [25,26]. Nanospace confinement can also create favorable conditions for the

electron transfer between CNTs and nanoparticles [27,28]. Hence, the electrochemical properties of Fe<sub>2</sub>O<sub>3</sub>(100)-in-CNTs and Fe<sub>2</sub>O<sub>3</sub>(100)-out-CNTs were evaluated. As compared with the Fe<sub>2</sub>O<sub>3</sub>(100)-out-CNTs, the Fe<sub>2</sub>O<sub>3</sub>(100)-in-CNTs exhibited larger current response in the curves of cyclic voltammetry (Fig. 4a), suggesting that the Fe<sub>2</sub>O<sub>3</sub>(100)-in-CNTs had a stronger capacity of electron transfer. Besides, the Tafel slope of Fe<sub>2</sub>O<sub>3</sub>(100)-in-CNTs (98.31 mV dec<sup>-1</sup>) was significantly lower than that of Fe<sub>2</sub>O<sub>3</sub>(100)-out-CNTs (197.01 mV dec<sup>-1</sup>), indicating faster catalytic reaction kinetics and better catalytic performance for the Fe<sub>2</sub>O<sub>3</sub>(100)-in-CNTs (Fig. 4b) [28]. As depicted in the Tafel polarization curves (Fig. 4c), the Fe<sub>2</sub>O<sub>3</sub>(100)-in-CNTs had a higher corrosion current and a lower corrosion potential, which was

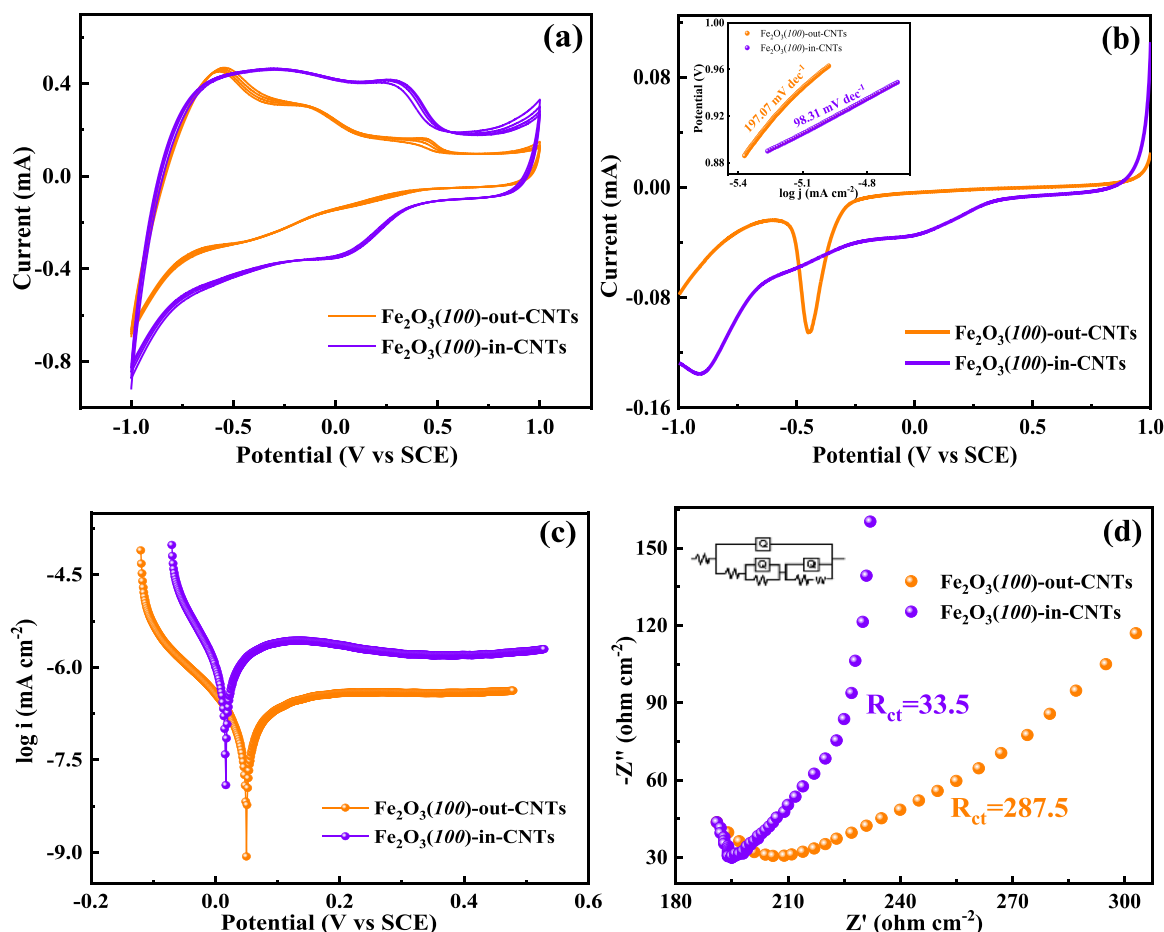


Fig. 4. Electrochemical properties of catalysts (a: CV curves; b: LSV curves; c: Tafel polarization curves; d: EIS).

prone to give away electrons and led to a faster electron transfer process [43]. The  $\text{Fe}_2\text{O}_3(100)\text{-in-CNTs}$  exhibited a smaller charge transfer resistance ( $R_{\text{ct}}$ ) value (Fig. 4d), demonstrating a lower transmission resistance during electron transfer process [44]. These above results demonstrated that the  $\text{Fe}_2\text{O}_3(100)\text{-in-CNTs}$  exhibited an excellent performance in the electron transfer compared with the  $\text{Fe}_2\text{O}_3(100)\text{-out-CNTs}$ . To further verify the importance of electron transfer, chemical scavenger of  $e^-$  was introduced into the NTP/ $\text{Fe}_2\text{O}_3(100)\text{-in-CNTs}$  system. As shown in Fig. 3a-b, there were 92.2% and 54.1% decreases in the reaction rate constant in the presence of  $e^-$  scavenger in the NTP/ $\text{Fe}_2\text{O}_3(100)\text{-in-CNTs}$  and NTP/ $\text{Fe}_2\text{O}_3(100)\text{-out-CNTs}$  systems, respectively. Thus, the electron transfer process was expedited by the  $\text{Fe}_2\text{O}_3(100)\text{-in-CNTs}$ , which then promoted Cu-EDTA decomposition.

### 3.3.4. DFT calculation on nanospace confinement effects

To further explore the regulatory effect of nanospace confinement, DFT calculation was conducted to analyze their microscopic chemical states and electron distribution, including Bader charge density,  $d$ -band theory and partial density of states (PDOS) of Fe 3d, O 2s, and C 1s. Fig. 5a depicts top views of the Bader charge density distribution of catalysts. The electron cloud was mainly distributed around  $\text{Fe}_2\text{O}_3$  and accumulated near CNTs in the  $\text{Fe}_2\text{O}_3(100)\text{-in-CNTs}$ ; however, it was uniformly distributed at  $\text{Fe}_2\text{O}_3$  surface in the  $\text{Fe}_2\text{O}_3(100)\text{-out-CNTs}$  conformation. More escaping electrons indicate that electrons are easy to be activated by transition and electron transfer [45]. Hence, the larger electron cloud in the  $\text{Fe}_2\text{O}_3(100)\text{-in-CNTs}$  proofed its higher catalytic activity and faster electron transfer, which were consistent with the experimental results. Electrons were transferred from the CNTs surface

to  $\text{Fe}_2\text{O}_3$  in the  $\text{Fe}_2\text{O}_3(100)\text{-in-CNTs}$  (Fig. 5b), resulting in the sharp increase in the Bader charge at Fe 1 (Fig. 5c). Interestingly, the electron density around majority of Fe atoms decreased in the  $\text{Fe}_2\text{O}_3(100)\text{-in-CNTs}$ . The shrinkage of the charge density around Fe is prone to form shorter Fe-O bonds, facilitating the formation of  $\text{Fe}^{\text{IV}}=\text{O}$  [46]. The EXAFS wavelet transform spectra also showed that a shorter Fe-O bonds (1.47 Å) occurred in the  $\text{Fe}_2\text{O}_3(100)\text{-in-CNTs}$  than in the  $\text{Fe}_2\text{O}_3(100)\text{-out-CNTs}$  (Fig. 5d-e). Furthermore,  $d$ -band theory and PDOS theory based on DFT calculation were also analyzed to explore the nanospace confinement effect at the atom level. As depicted in Fig. 5f-g, the  $d$ -band center of the nanospace confined  $\text{Fe}_2\text{O}_3$  shifted from  $-3.30$  eV to a higher energy of  $-3.10$  eV, which meant that more antibonding states of adsorbed intermediates existed above the Fermi level, leading to the enhancement of their binding strength [47]. Hence, the adsorption capacities for  $\text{H}_2\text{O}_2$  and  $\text{O}_3$  would be strengthened by the  $\text{Fe}_2\text{O}_3(100)\text{-in-CNTs}$ , promoting the ROS formation and Cu-EDTA decomposition. Additionally, compared with the  $\text{Fe}_2\text{O}_3(100)\text{-out-CNTs}$  (Fig. 5g), the 3d orbital electrons of the Fe atom were inclined to accumulate near the Fermi level in the  $\text{Fe}_2\text{O}_3(100)\text{-in-CNTs}$ , as well as O 2s and C 1s orbital electrons (Fig. 5f), suggesting a stronger chemical reactivity [48]. Moreover, the orbital electrons of the Fe 3d, O 2s, and C 1s had higher overlaps in the  $\text{Fe}_2\text{O}_3(100)\text{-in-CNTs}$  conformation (Fig. 5f), which indicated that more electrons were in a similar energy level, thus they were prone to electron transfer [49].

In summary, different mechanisms of the  $\text{Fe}_2\text{O}_3(100)\text{-in-CNTs}$  and  $\text{Fe}_2\text{O}_3(100)\text{-out-CNTs}$  are proposed in Fig. 6. After nanoconfinement, the localization of electron distribution on the surface of  $\text{Fe}_2\text{O}_3$  resulted in faster electron transfer and stronger adsorption capacities between active sites and  $\text{H}_2\text{O}_2$  and/or  $\text{O}_3$ , and the shrinkage of the charge density



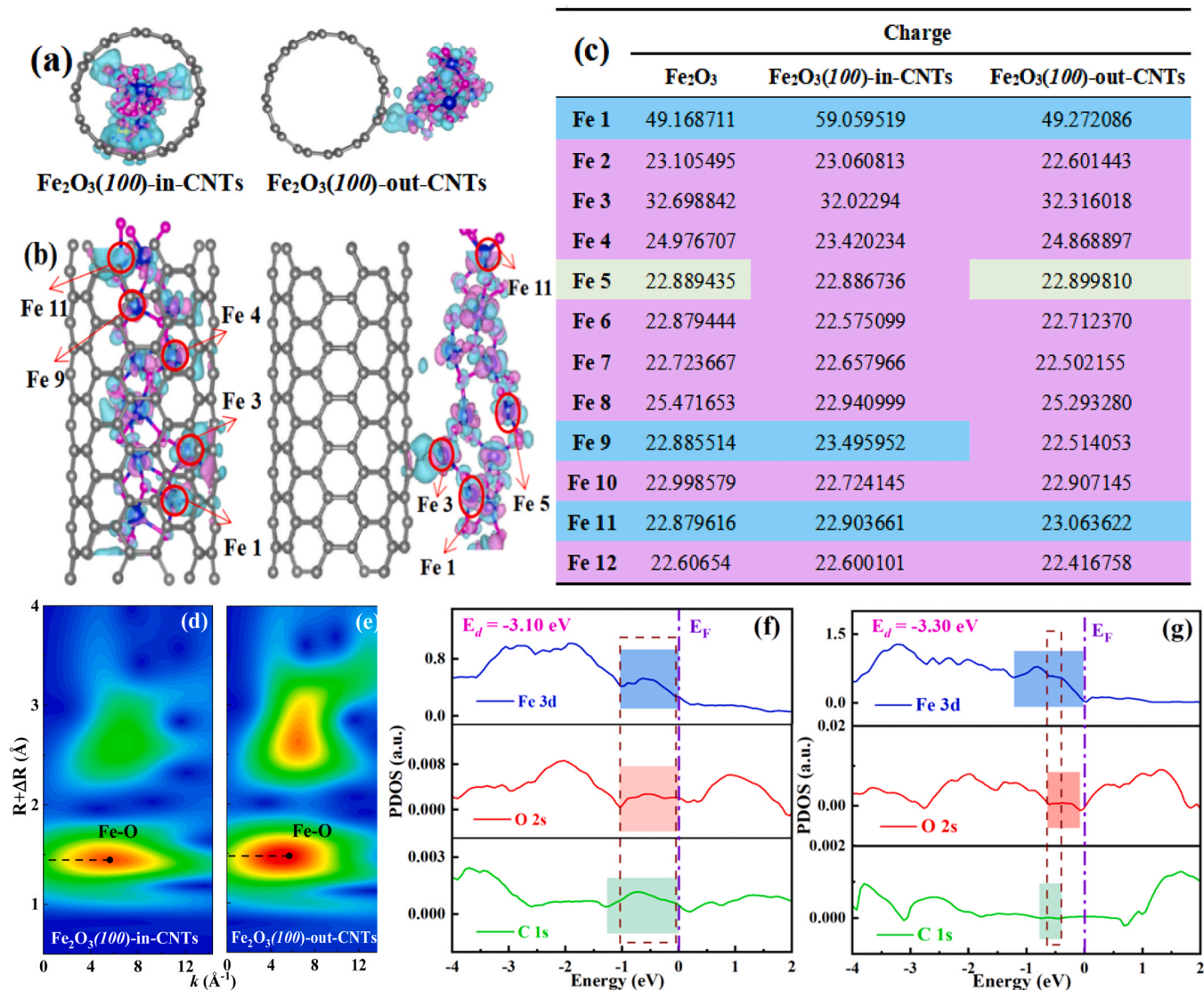
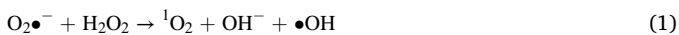


Fig. 5. Bader charge density distribution of Fe<sub>2</sub>O<sub>3</sub>(100)-in-CNTs and Fe<sub>2</sub>O<sub>3</sub>(100)-out-CNTs (a-b); Bader charge (c); EXAFS wavelet transform spectra of Fe<sub>2</sub>O<sub>3</sub>(100)-in-CNTs (d) and Fe<sub>2</sub>O<sub>3</sub>(100)-out-CNTs (e); PDOS of Fe 3d, O 2s, and C 1s of Fe<sub>2</sub>O<sub>3</sub>(100)-in-CNTs (f) and Fe<sub>2</sub>O<sub>3</sub>(100)-out-CNTs (g).

around Fe atoms induced by the nanospace confinement effect also promoted Fe<sup>IV</sup>=O formation. Moreover, the interactions between ROS were enhanced due to spatial confinement by CNTs, thus leading to more <sup>1</sup>O<sub>2</sub> formation as Eqs. (1–4) (Fig. 3) and a non-radical dominant pathway of Cu-EDTA removal in the Fe<sub>2</sub>O<sub>3</sub>(100)-in-CNTs system. Therefore, these theoretical evidences further demonstrated the unique advantages of the nanospace confined structure.



### 3.3.5. Cu-EDTA decomposition process

For the UV-vis spectra in Fig. 7a, the peak around 268 nm was related to Cu-EDTA, and it decreased after treatment by NTP/Fe<sub>2</sub>O<sub>3</sub>(100)-in-CNTs, resulting from Cu-EDTA decomposition [5]. Correspondingly, the characteristic peak at 195 nm consistent with the peak of Cu<sup>2+</sup> obviously increased, which further demonstrated the

decomposition of Cu-EDTA, leading to Cu<sup>2+</sup> release. Some small organic substances (including acetic acid, N,N-diethylformamide, acetamide, ethylene glycol, formamide, lactic acid, ethanamine, 1,3-butanediol, ethanol, and diglycolic acid) were detected by GC-MS in the nanospace confined system, as listed in Table S5. Formic acid, acetic acid, and NO<sub>3</sub> were all gradually accumulated in the Cu-EDTA decomposition process (Fig. 7b), which accompanied by 53% of total organic carbon (TOC) removal within 20 min (Fig. S12). Compared with the systems of NTP and NTP/Fe<sub>2</sub>O<sub>3</sub>(100)-in-CNTs, there were 33% and 19% increases in the TOC removal in the NTP/Fe<sub>2</sub>O<sub>3</sub>(100)-in-CNTs system, respectively.

The Cu-EDTA decomposition pathways were proposed in Fig. 7c. For pathway ①, byproducts P6 and P5 were generated by attacks of ROS to the C-N bonds of Cu-EDTA. Previous studies reported that ROS easily destroyed the C-N bonds in-N-(CH<sub>2</sub>-COOH)<sub>2</sub> [4,8]. The C-N bonds in P6 were broken by ROS to produce byproducts P7 and P2, and then those nitrogenous organics were oxidized to byproduct P4 via carbon-ylolation process. Previous studies also reported that low molecular substances (such as ethylene glycol, glycine, acetic acid, 1,3-butanediol and lactic acid) were generated during EDTA-chelated complexes removal process [8,9,29]. For pathway ②, byproduct P9 was decomposed to byproducts P10 and P8 under the attacks of ROS, producing smaller



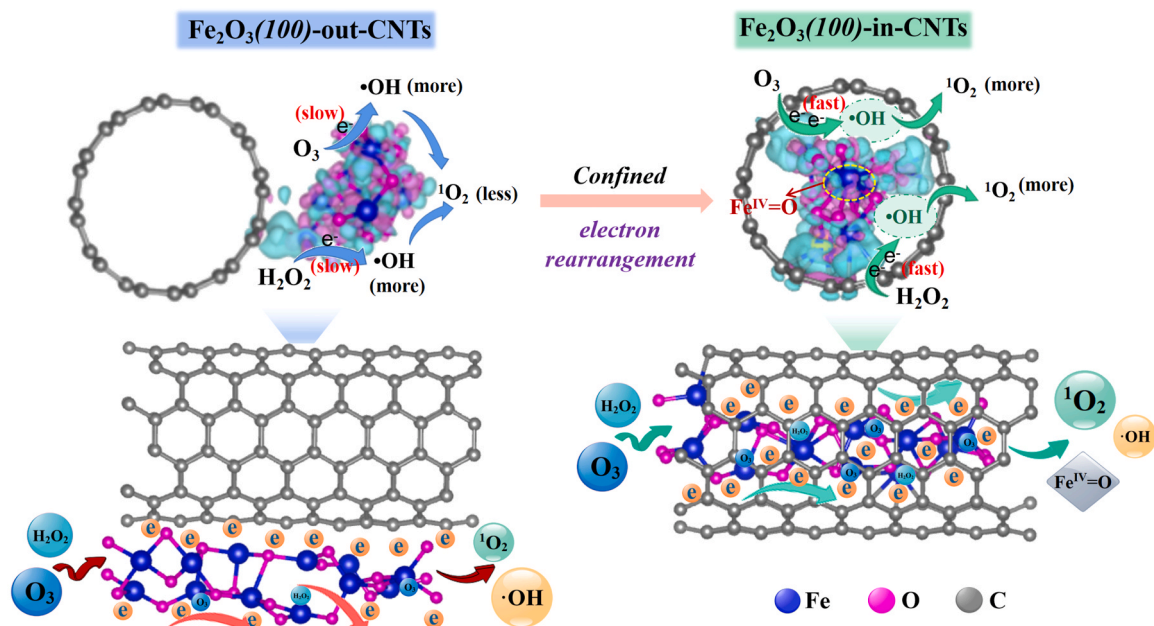


Fig. 6. Schematic diagram of catalytic mechanisms of  $\text{Fe}_2\text{O}_3(100)\text{-out-CNTs}$  and  $\text{Fe}_2\text{O}_3(100)\text{-in-CNTs}$ .

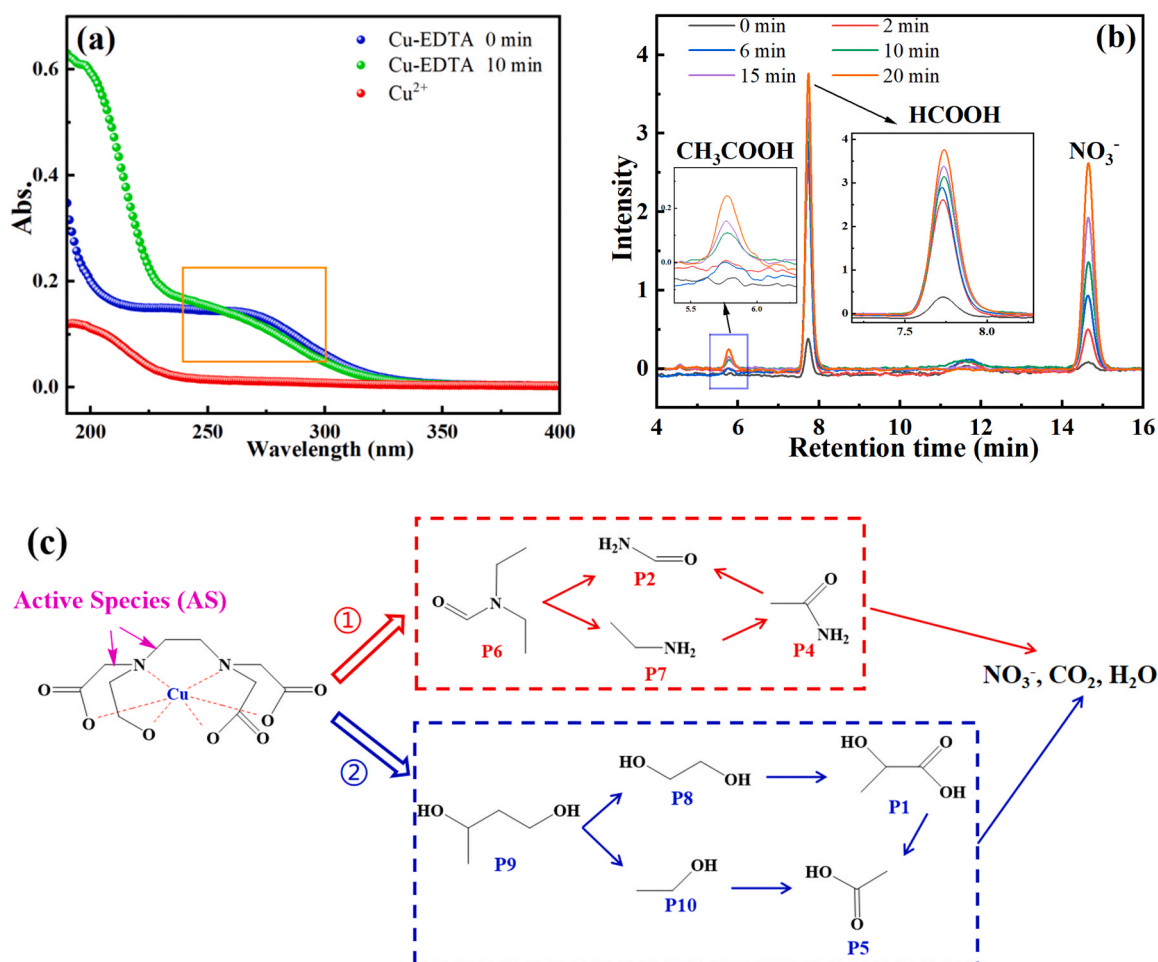


Fig. 7. Cu-EDTA decomposition process in the NTP/ $\text{Fe}_2\text{O}_3(100)\text{-in-CNTs}$  system (a: UV-vis spectra; b: ion chromatography; c: possible decomposition pathways. P1-P10 are the byproducts listed in Table S3. Catalyst dosage =  $0.1 \text{ g L}^{-1}$ .  $[\text{Cu-EDTA}]_0 = 0.05 \text{ mmol L}^{-1}$ . Voltage = 12 kV).

alcohols, and then oxidized to byproducts P1 and P5 by carboxylation process. In general, Cu-EDTA decomposition is an oxidation process of continuous hydroxylation and carboxylation [4]. Finally, those intermediate byproducts were mineralized to  $\text{NO}_3^-$ ,  $\text{CO}_2$ , and  $\text{H}_2\text{O}$  under continuous oxidation [8,9,14,29].

### 3.4. Stability and applicability of NTP/ $\text{Fe}_2\text{O}_3(100)$ -in-CNTs

Fig. 8a depicts the stability of the NTP/ $\text{Fe}_2\text{O}_3(100)$ -in-CNTs system. Cu-EDTA removal efficiency was still kept approximately 100% after four cycles. There was no obvious changes in the XRD spectra of the used  $\text{Fe}_2\text{O}_3(100)$ -in-CNTs, as compared with the raw  $\text{Fe}_2\text{O}_3(100)$ -in-CNTs (Fig. S13). The total Fe content just decreased by 0.53% in the used  $\text{Fe}_2\text{O}_3(100)$ -in-CNTs (Table S6). The XPS of Fe 2p of the used  $\text{Fe}_2\text{O}_3(100)$ -in-CNTs still exhibited the coexistent of Fe(III) and Fe(II), and slight decrease in the Fe(II) proportion was observed (Fig. 8b), compared with the raw  $\text{Fe}_2\text{O}_3(100)$ -in-CNTs (Fig. 11). Thus, the prepared  $\text{Fe}_2\text{O}_3(100)$ -in-CNTs catalyst exhibited a great stability.

The Cu-EDTA removal performances with additions of humic acid (HA,  $10 \text{ mg L}^{-1}$ ) and different inorganic anions ( $0.1 \text{ mmol L}^{-1}$ ) in the NTP/ $\text{Fe}_2\text{O}_3(100)$ -in-CNTs system were evaluated. Nearly 100% of Cu-EDTA was still removed within 20 min treatment with the addition of  $\text{Cl}^-$ ,  $\text{SO}_4^{2-}$ , and  $\text{NO}_3^-$ , while  $\text{CO}_3^{2-}$ ,  $\text{PO}_4^{3-}$ , and HA slightly inhibited this process because of the shielding of ROS and competing reactions (Fig. 8c) [3,50]. Meanwhile, the NTP/ $\text{Fe}_2\text{O}_3(100)$ -in-CNTs system still had satisfactory performances (more than 95% within 20 min) for

Cu-EDTA elimination in the tap water and river water (Fig. 8c). Moreover, several types of organic pollutants, including dyes (MB and MO), antibiotics (SD and CIP), nitrobenzene (NB), phenol, and other metal complexes (Fe-EDTA and Ni-EDTA), were also selected to evaluate the applicability of the NTP/ $\text{Fe}_2\text{O}_3(100)$ -in-CNTs system. As shown in Fig. 8d, the removal efficiencies of these organic pollutants reached 83%–100% after 20 min of treatment. Hence, the NTP/ $\text{Fe}_2\text{O}_3(100)$ -in-CNTs system had a great environmental applicability.

## 4. Conclusions

Nanospace confined catalyst ( $\text{Fe}_2\text{O}_3(100)$ -in-CNTs) was successfully synthesized, and it presented more active sites, better catalytic performance, and a stronger capacity of electron transfer, compared with unconfined catalyst ( $\text{Fe}_2\text{O}_3(100)$ -out-CNTs). The coupling of NTP/ $\text{Fe}_2\text{O}_3(100)$ -in-CNTs displayed superbly high catalytic activity with 98.8% of Cu-EDTA decomplexation within 20 min; correspondingly, the kinetic constant was 2.5 times of the NTP/ $\text{Fe}_2\text{O}_3(100)$ -out-CNTs. The localization of electron distribution on  $\text{Fe}_2\text{O}_3$  surface and the shrinkage of the charge density around Fe atoms induced by the nanospace confinement effect promoted formation of highly oxidative  $\text{Fe}^{\text{IV}}=\text{O}$ ; the rearrangement of orbital electrons also facilitated ROS adsorption and electron transfer, thus promoting Cu-EDTA decomplexation. Different from radical pathway dominated by  $\bullet\text{OH}$  in the NTP/ $\text{Fe}_2\text{O}_3(100)$ -out-CNTs system, non-radical pathway ( $^1\text{O}_2$  and  $\text{Fe}^{\text{IV}}=\text{O}$ ) dominated Cu-

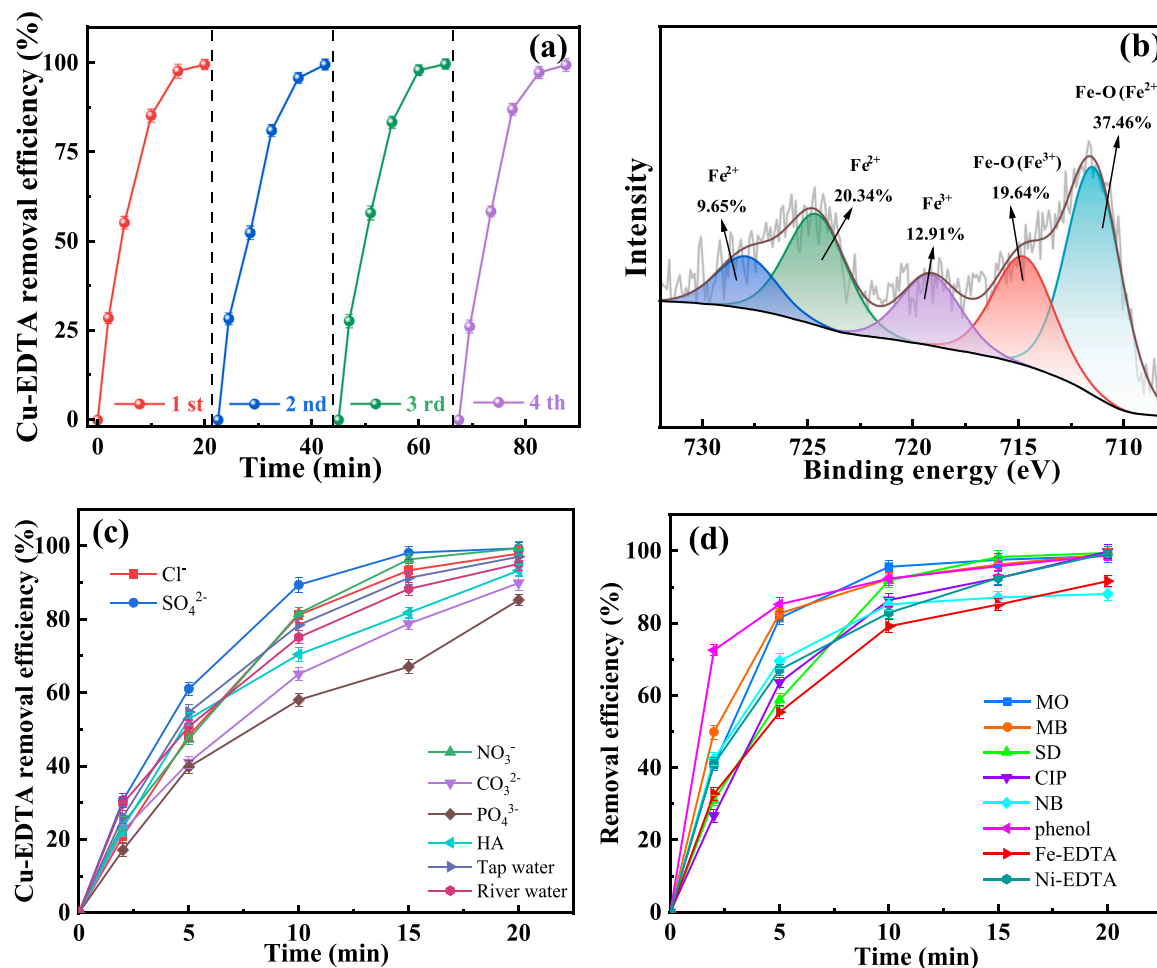


**Fig. 8.** Reusability of  $\text{Fe}_2\text{O}_3(100)$ -in-CNTs on Cu-EDTA removal (a); XPS of Fe 2p of used  $\text{Fe}_2\text{O}_3(100)$ -in-CNTs (b); influences of HA, different ions, and water matrix on Cu-EDTA removal (c); removal of different pollutants in NTP/ $\text{Fe}_2\text{O}_3(100)$ -in-CNTs system (d) (Catalyst dosage =  $0.1 \text{ g L}^{-1}$ ,  $[\text{Cu-EDTA}]_0 = 0.05 \text{ mmol L}^{-1}$ . Voltage = 12 kV. methylene blue, MB; methyl orange, MO; sulfadiazine, SD; ciprofloxacin, CIP; NB: nitrobenzene).

EDTA decomplexation in the NTP/Fe<sub>2</sub>O<sub>3</sub>(100)-in-CNTs system. These ROS broke C-N bonds in-N-(CH<sub>2</sub>-COOH)<sub>2</sub> groups in Cu-EDTA, initiating the decomplexation process. Furthermore, the Fe<sub>2</sub>O<sub>3</sub>(100)-in-CNTs exhibited a great stability and environmental applicability.

### CRedit authorship contribution statement

**Zhang Ying:** Conceptualization, Methodology, Software. **Zhou Jian:** Formal analysis, Methodology, Software, Supervision. **Li Anjie:** Investigation, Visualization. **Yang Yueyun:** Investigation, Visualization. **Liu Yue:** Writing – original draft, Writing – review & editing, Investigation, Methodology. **Zhu Lingyan:** Project administration, Supervision, Writing – review & editing. **Jia Hanzhong:** Project administration, Validation. **Wang Tiecheng:** Formal analysis, Funding acquisition, Project administration, Writing – review & editing.

### Declaration of Competing Interest

There is no conflict of interest between the authors.

### Data Availability

Data will be made available on request.

### Acknowledgments

National Natural Science Foundation of China (No. 42377388) supported this research.

### Appendix A. Supporting information

Supplementary data associated with this article can be found in the online version at [doi:10.1016/j.apcatb.2024.123717](https://doi.org/10.1016/j.apcatb.2024.123717).

### References

- Z.L. Li, J. Chen, H.Y. Guo, X. Fan, Z. Wen, M.H. Yeh, C.W. Yu, X. Cao, Z.L. Wang, Triboelectrification-enabled self-powered detection and removal of heavy metal ions in wastewater, *Adv. Mater.* 28 (2016) 2983–2991, <https://doi.org/10.1002/adma.201504356>.
- M.Q. Li, H. Shang, H. Li, Y.F. Hong, C.C. Ling, K. Wei, B.A. Zhou, C.L. Mao, Z.H. Ai, L.Z. Zhang, Kirkendall effect boosts phosphorylated nZVI for efficient heavy metal wastewater treatment, *Angew. Chem. Int. Ed.* 60 (2021) 17115–17122, <https://doi.org/10.1002/anie.202104586>.
- Y. Liu, T.C. Wang, G.Z. Qu, H.Z. Jia, High-efficient decomplexation of Cu-HA by discharge plasma: Process and mechanisms, *Sep. Purif. Technol.* 248 (2020) 117137–117146, <https://doi.org/10.1016/j.seppur.2020.117137>.
- S.W. Xie, W. Shao, H. Zhan, Z. Wang, C.C. Ge, Q.J. Li, W.J. Fu, Cu(II)-EDTA removal by a two-step Fe(0) electrocoagulation in near natural water: Sequent transformation and oxidation of EDTA complexes, *J. Hazard. Mater.* 392 (2020) 122473–122481, <https://doi.org/10.1016/j.jhazmat.2020.122473>.
- T.C. Wang, Q. Wang, H. Soklun, G.Z. Qu, T.J. Xia, X.T. Guo, H.Z. Jia, L.Y. Zhu, A green strategy for simultaneous Cu(II)-EDTA decomplexation and Cu precipitation from water by bicarbonate-activated hydrogen peroxide/chemical precipitation, *Chem. Eng. J.* 370 (2019) 1298–1309, <https://doi.org/10.1016/j.cej.2019.04.005>.
- Z. Xu, G.D. Gao, B.C. Pan, W.M. Zhang, L. Lv, A new combined process for efficient removal of Cu(II) organic complexes from wastewater: Fe(III) displacement/UV degradation/alkaline precipitation, *Water Res.* 87 (2015) 378–384, <https://doi.org/10.1016/j.watres.2015.09.025>.
- W. Guan, B.F. Zhang, S.C. Tian, X. Zhao, The synergism between electro-Fenton and electrocoagulation process to remove Cu-EDTA, *Appl. Catal. B: Environ.* 227 (2018) 252–257, <https://doi.org/10.1016/j.apcatb.2017.12.036>.
- X.F. Huang, Y. Xu, C. Shan, X.C. Li, W.M. Zhang, B.C. Pan, Coupled Cu(II)-EDTA degradation and Cu(II) removal from acidic wastewater by ozonation: performance, products and pathways, *Chem. Eng. J.* 299 (2016) 23–29, <https://doi.org/10.1016/j.cej.2016.04.044>.
- S.T. He, T.F. Li, L. Zhang, X.F. Zhang, Z.W. Liu, Y. Zhang, J.Z. Wang, H.Z. Jia, T. C. Wang, L.Y. Zhu, Highly effective photocatalytic decomplexation of Cu-EDTA by MIL-53(Fe): highlight the important roles of Fe, *Chem. Eng. J.* 424 (2021) 130515, <https://doi.org/10.1016/j.cej.2021.130515>.
- D.Y. Zu, H.R. Song, C.P. Li, Y.W. Wang, R. Du, R. Zhou, W. Zhang, S.T. Pan, Y. Cai, Y.M. Shen, Z.F. Yang, Understanding the self-catalyzed decomplexation mechanism of Cu-EDTA in Ti<sub>3</sub>C<sub>2</sub>T<sub>x</sub> MXene/peroxymonosulfate process, *Appl. Catal. B-Environ.* 306 (2022) 121131, <https://doi.org/10.1016/j.apcatb.2022.121131>.
- M.Q. Li, N. Chen, H. Shang, C.C. Ling, K. Wei, S.X. Zhao, B. Zhou, F.L. Jia, Z.H. Ai, L.Z. Zhang, An electrochemical strategy for simultaneous heavy metal complexes wastewater treatment and resource recovery, *Environ. Sci. Technol.* 56 (2022) 10945–10953, <https://doi.org/10.1021/acs.est.2c02363>.
- W.C. Xu, X.D. Jiang, H.H. Chen, X. Chen, L.M. Chen, J.L. Wu, M.L. Fu, D.Q. Ye, Adsorption-discharge plasma system for toluene decomposition over Ni-SBA catalyst: In situ observation and humidity influence study, *Chem. Eng. J.* 382 (2020) 122950, <https://doi.org/10.1016/j.cej.2019.122950>.
- N. Jiang, X.C. Li, H. Guo, J. Li, K.F. Shang, N. Lu, Y. Wu, Plasma-assisted catalysis decomposition of BPA over graphene-CdS nanocomposites in pulsed gas-liquid hybrid discharge: Photocorrosion inhibition and synergistic mechanism analysis, *Chem. Eng. J.* 412 (2021) 128627–128641, <https://doi.org/10.1016/j.cej.2021.128627>.
- T.C. Wang, Y. Cao, G.Z. Qu, Q.H. Sun, T.J. Xia, X.T. Guo, H.Z. Jia, L.Y. Zhu, Novel Cu(II)-EDTA decomplexation by discharge plasma oxidation and coupled Cu removal by alkaline precipitation: Underneath mechanisms, *Environ. Sci. Technol.* 52 (2018) 7884–7891, <https://doi.org/10.1021/acs.est.8b02039>.
- S. Chen, H.Q. Wang, F. Dong, Activation and characterization of environmental catalysts in plasma-catalysis: Status and challenges, *J. Hazard. Mater.* 427 (2022) 128150–128175, <https://doi.org/10.1016/j.jhazmat.2021.128150>.
- T. Wang, S. Chen, H.G. Wang, Z. Liu, Z.B. Wu, In-plasma catalytic degradation of toluene over different MnO<sub>2</sub> polymorphs study of reaction mechanism, *Chin. J. Catal.* 38 (2017) 793–804, [https://doi.org/10.1016/S1872-2067\(17\)62808-0](https://doi.org/10.1016/S1872-2067(17)62808-0).
- F. Holzer, U. Roland, F.D. Kopinke, Combination of non-thermal plasma and heterogeneous catalysis for oxidation of volatile organic compounds Part 1. Accessibility of the intra-particle volume, *Appl. Catal. B-Environ.* 38 (2002) 163–181, [https://doi.org/10.1016/S0926-3373\(02\)00040-1](https://doi.org/10.1016/S0926-3373(02)00040-1).
- H. Guo, Y.W. Wang, L.N. Liao, Z. Li, S.J. Pan, C.D. Puyang, Y.Y. Su, Y. Zhang, T. C. Wang, J.Y. Ren, J. Li, Review on remediation of organic-contaminated soil by discharge plasma: plasma types, impact factors, plasma-assisted catalysis, and indexes for remediation, *Chem. Eng. J.* 436 (2022) 135239–135260, <https://doi.org/10.1016/j.cej.2022.135239>.
- H.Y. Niu, D.W. He, Y.L. Yang, H.Z. Lv, Y.Q. Cai, Y. Liang, Long-lasting activity of Fe<sup>0</sup>-C internal microelectrolysis-Fenton system assisted by Fe/C-montmorillonites nanocomposites, *Appl. Catal. B-Environ.* 256 (2019) 117820–117830, <https://doi.org/10.1016/j.apcatb.2019.117820>.
- Z.P. Hao, D.Y. Cheng, Y. Guo, Y.H. Liang, Supported gold catalysts used for ozone decomposition and simultaneous elimination of ozone and carbon monoxide at ambient temperature, *Appl. Catal. B-Environ.* 33 (2001) 217–222, [https://doi.org/10.1016/S0926-3373\(01\)00172-2](https://doi.org/10.1016/S0926-3373(01)00172-2).
- J.-B. Tarkwa, E. Acayanka, B. Jiang, N. Oturan, G.Y. Kamgang, S. Laminsi, M. A. Oturan, Highly efficient degradation of azo dye Orange G using laterite soil as catalyst under irradiation of non-thermal plasma, *Appl. Catal. B-Environ.* 246 (2019) 211–220, <https://doi.org/10.1016/j.apcatb.2019.01.066>.
- Y. Chen, G. Zhang, H.J. Liu, J.H. Qu, Confining free radicals in close vicinity to contaminants enables ultrafast Fenton-like processes in the interspersing of MoS<sub>2</sub> membranes, *Angew. Chem. Int. Ed.* 58 (2019) 8134–8138, <https://doi.org/10.1002/anie.201903531>.
- S. Zhang, T. Hedtke, X.C. Zhou, M. Elimelech, J.H. Kim, Environmental applications of engineered materials with nanoconfinement, *ACS EST Eng.* 1 (2021) 706–724, <https://doi.org/10.1021/acsesteng.1c00007>.
- S. Zhang, T. Hedtke, L. Wang, X.X. Wang, T.C. Cao, M. Elimelech, J.H. Kim, Engineered nanoconfinement accelerating spontaneous manganese-catalyzed degradation of organic contaminants, *Environ. Sci. Technol.* 55 (2021) 16708–16715, <https://doi.org/10.1021/acs.est.1c06551>.
- R.L. Zhu, Y.P. Zhu, H.Y. Xian, L.X. Yan, H.Y. Fu, G.Q. Zhu, Y.F. Xi, J.X. Zhu, H. P. He, CNTs/ferrihydrite as a highly efficient heterogeneous Fenton catalyst for the degradation of bisphenol A: The important role of CNTs in accelerating Fe(III)/Fe(II) cycling, *Appl. Catal. B-Environ.* 270 (2020) 118891–118901, <https://doi.org/10.1016/j.apcatb.2020.118891>.
- P. Su, W.Y. Fu, X.D. Du, G. Song, Y.P. Tang, M.H. Zhou, Nanoscale confinement in carbon nanotubes encapsulated zero-valent iron for phenolics degradation by heterogeneous Fenton: Spatial effect and structure–activity relationship, *Sep. Purif. Technol.* 276 (2021) 119232–119246, <https://doi.org/10.1016/j.seppur.2021.119232>.
- D.L. Guo, Y. Yao, S.J. You, L.M. Jin, P. Lu, Y.B. Liu, Ultrafast degradation of micropollutants in water via electro-periodate activation catalyzed by nanoconfined Fe<sub>2</sub>O<sub>3</sub>, *Appl. Catal. B: Environ.* 309 (2022) 121289–121299, <https://doi.org/10.1016/j.apcatb.2022.121289>.
- D.L. Guo, Y.B. Liu, H.D. Ji, C.C. Wang, B. Chen, C.S. Shen, F. Li, Y.X. Wang, P. Lu, W. Liu, Silicate-enhanced heterogeneous flow-through electro-Fenton system using iron oxides under nanoconfinement, *Environ. Sci. Technol.* 55 (2021) 4045–4053, <https://doi.org/10.1021/acs.est.1c00349>.
- Y. Liu, M.Q. Lu, Y.R. Yin, J. Zhou, G.Z. Qu, Y. Zhang, H. Guo, S.F. Tang, C. Liu, T. C. Wang, Self-catalytic Fenton-like reactions stimulated synergistic Cu-EDTA decomplexation and Cu recovery by glow plasma electrolysis, *Chem. Eng. J.* 433 (2022) 134601–134612, <https://doi.org/10.1016/j.cej.2022.134601>.
- H. Bader, J. Hoigné, Determination of ozone in water by the indigo method, *Water Res.* 15 (1981) 449–456, [https://doi.org/10.1016/0043-1354\(81\)90054-3](https://doi.org/10.1016/0043-1354(81)90054-3).
- Z. Wang, J. Jiang, S.Y. Pang, Y. Zhou, C.T. Guan, Y. Gao, J. Li, Y. Yang, W. Qu, C. C. Jiang, Is sulfate radical really generated from peroxydisulfate activated by Iron (II) for environmental decontamination? *Environ. Sci. Technol.* 52 (2018) 11276–11284, <https://doi.org/10.1021/acs.est.8b02266>.

- [32] L. Chen, S. Wang, Z.C. Yang, J.S. Qian, B.C. Pan, Selective interfacial oxidation of organic pollutants in Fenton-like system mediated by Fe(III)-adsorbed carbon nanotubes, *Appl. Catal. B-Environ.* 292 (2021) 120193–120202, <https://doi.org/10.1016/j.apcatb.2021.120193>.
- [33] G.E. Bialek-Bylka, K. Pawlak, B. Jazurek, A. Skrzypczak, Y. Koyama, Spectroscopic properties and temperature induced electronic configuration changes of all-trans and 15-cis beta-carotenes in ionic liquids, *Photosynthetica* 45 (2007) 161–166, <https://doi.org/10.1007/s11099-007-0027-z>.
- [34] C.Y. Zhou, P. Zhou, M.L. Sun, Y. Liu, H. Zhang, Z.K. Xiong, J. Liang, X.G. Duan, B. Lai, Nitrogen-doped carbon nanotubes enhanced Fenton chemistry: Role of near-free iron(III) for sustainable iron(III)/iron(II) cycles, *Water Res.* 210 (2022) 117984–117994, <https://doi.org/10.1016/j.watres.2021.117984>.
- [35] T.I.T. Okpalugo, P. Papakonstantinou, H. Murphy, J. McLaughlin, N.M.D. Brown, High resolution XPS characterization of chemical functionalised MWCNTs and SWCNTs, *Carbon* 43 (2005) 153–161, <https://doi.org/10.1016/j.carbon.2004.08.033>.
- [36] B. Li, X.L. Cheng, R.S. Zou, X.Y. Yong, C.F. Pang, Y.Y. Su, Y.F. Zhang, Simple modulation of Fe-based single atoms/clusters catalyst with acidic microenvironment for ultrafast Fenton-like reaction, *Appl. Catal. B: Environ.* 304 (2022) 121009–121019, <https://doi.org/10.1016/j.apcatb.2021.121009>.
- [37] Y.P. Long, J.T. Nie, C.C. Yuan, H. Ma, Y.Q. Chen, Y.Q. Cong, Q. Wang, Y. Zhang, Preparation of CoFe<sub>2</sub>O<sub>4</sub>/MWNTs/sponge electrode to enhance dielectric barrier plasma discharge for degradation of phenylic pollutants and Cr(VI) reduction, *Appl. Catal. B-Environ.* 283 (2021) 119604–119616, <https://doi.org/10.1016/j.apcatb.2020.119604>.
- [38] Z.L. Song, M.X. Wang, Z. Wang, Y.F. Wang, R.Y. Li, Y.T. Zhang, C. Liu, Y. Liu, B. B. Xu, F. Qi, Insights into heteroatom-doped graphene for catalytic ozonation: Active centers, reactive oxygen species evolution, and catalytic mechanism, *Environ. Sci. Technol.* 53 (2019) 5337–5348, <https://doi.org/10.1021/acs.est.9b01361>.
- [39] G.S. Xia, Y.J. Wang, B. Wang, J. Huang, S.B. Deng, G. Yu, The competition between cathodic oxygen and ozone reduction and its role in dictating the reaction mechanisms of an electro-peroxone process, *Water Res.* 118 (2017) 26–38, <https://doi.org/10.1016/j.watres.2017.04.005>.
- [40] C. Zhang, M.H. Zhou, G.B. Ren, X.M. Yu, L. Ma, J. Yang, F.K. Yu, Heterogeneous electro-Fenton using modified iron-carbon as catalyst for 2,4-dichlorophenol degradation: Influence factors, mechanism and degradation pathway, *Water Res.* 70 (2015) 414–424, <https://doi.org/10.1016/j.watres.2014.12.022>.
- [41] B.B. Shao, H.Y. Dong, B. Sun, X.H. Guan, Role of Ferrate(IV) and Ferrate(V) in activating Ferrate(VI) by calcium sulfite for enhanced oxidation of organic contaminants, *Environ. Sci. Technol.* 53 (2019) 894–902, <https://doi.org/10.1021/acs.est.8b04990>.
- [42] X.J. Zhang, X.B. Zhu, H. Li, C.H. Wang, T.T. Zhang, Combination of peroxymonosulfate and Fe(VI) for enhanced degradation of sulfamethoxazole: The overlooked roles of high-valent iron species, *Chem. Eng. J.* 453 (2023) 139742–139751, <https://doi.org/10.1016/j.cej.2022.139742>.
- [43] Y. Mu, Z.H. Ai, L.Z. Zhang, Phosphate shifted oxygen reduction pathway on Fe@Fe<sub>2</sub>O<sub>3</sub> core-shell nanowires for enhanced reactive oxygen species generation and aerobic 4-chlorophenol degradation, *Environ. Sci. Technol.* 51 (2017) 8101–8109, <https://doi.org/10.1021/acs.est.7b01896>.
- [44] J.R. Barbosa, M.N. Leon, C.M. Fernandes, R.M. Antoniassi, O.C. Alves, E.A. Ponzio, J.C.M. Silva, PtSnO<sub>2</sub>/C and Pt/C with preferential (100) orientation: High active electrocatalysts for ammonia electro-oxidation reaction, *Appl. Catal. B: Environ.* 264 (2020) 118458–118465, <https://doi.org/10.1016/j.apcatb.2019.118458>.
- [45] D.H. Li, B.B. Wang, X.J. Long, W.J. Xu, Y.Z. Xia, D.J. Yang, X.D. Yao, Controlled asymmetric charge distribution of active centers in conjugated polymers for oxygen reduction, *Angew. Chem. Int. Ed.* 60 (2021) 26483–26488, <https://doi.org/10.1002/anie.202109057>.
- [46] B.B. Shao, Y. Hong, B. Sun, X.H. Guan, Role of Ferrate(IV) and Ferrate(V) in activating Ferrate(VI) by calcium sulfite for enhanced oxidation of organic contaminants, *Environ. Sci. Technol.* 53 (2019) 894–902, <https://doi.org/10.1021/acs.est.8b04990>.
- [47] P.L. Zhai, M.Y. Xia, Y.Z. Wu, G.H. Zhang, J.F. Gao, B. Zhang, S.Y. Cao, Y.T. Zhang, Z.W. Li, Z.Z. Fan, C. Wang, X.M. Zhang, J.T. Miller, L.C. Sun, J.G. Hou, Engineering single-atomic ruthenium catalytic sites on defective nickel-iron layered double hydroxide for overall water splitting, *Nat. Commun.* 12 (2021) 4587–4589, <https://doi.org/10.1038/s41467-021-24828-9>.
- [48] X.Y. Zhang, S. Zhang, Y. Yang, L.G. Wang, Z.J. Mu, H.S. Zhu, X.Q. Zhu, H.H. Xing, H.Y. Xia, B.L. Huang, J. Li, S.J. Guo, E.K. Wang, A general method for transition metal single atoms anchored on honeycomb-like nitrogen-doped carbon nanosheets, *Adv. Mater.* 32 (2020) 1906905–1906913, <https://doi.org/10.1002/adma.201906905>.
- [49] G.B. Wen, D.U. Lee, B.H. Ren, F.M. Hassan, G.P. Jiang, Z.P. Cano, J. Gostick, E. Croiset, Z.Y. Bai, L. Yang, Z.W. Chen, Orbital interactions in Bi-Sn bimetallic electrocatalysts for highly selective electrochemical CO<sub>2</sub> reduction toward formate production, *Adv. Energy Mater.* 8 (2018) 1802427–1802436, <https://doi.org/10.1002/aenm.201802427>.
- [50] X.K. Zhang, J.H. Liu, X.C. Zheng, R. Chen, M. Zhang, Z.Y. Liu, Z.Y. Wang, J. Li, Activation of oxalic acid via dual-pathway over single-atom Fe catalysts: mechanism and membrane application, *Appl. Catal. B: Environ.* 321 (2023) 122068–122079, <https://doi.org/10.1016/j.apcatb.2022.122068>.